Investigation of Factors Affecting Iced-Airfoil Aerodynamics

Sam Lee* and Michael B. Bragg[†]

University of Illinois at Urbana-Champaign, Urbana, Illinois 61801

A summary of the effects the ice-accretion geometry, size, and location; the airfoil geometry; and the flight Reynolds number on iced-airfoil aerodynamics, based on the findings of the recent University of Illinois investigations, is presented. Four airfoils were tested with simulated glaze-ice horn and spanwise ridge ice. Increasing the ice-shape height generally resulted in more severe performance degradation. The exception was when the ice shape was located at the leading edge of the airfoil, where increased ice-shape height did not significantly degrade performance. Varying the leading-edge radius of glaze-ice horn did not have a large effect on airfoil performance. The variations in the geometry of the simulated ridge ice had some effect on airfoil aerodynamics, with (of the shapes tested) the half-round shape having a significantly higher maximum lift. Iced-airfoil aerodynamics were relatively insensitive to Reynolds number variations. Large differences in iced-airfoil aerodynamics were observed between different airfoil geometries. The findings showed that an airfoil's sensitivity to ridge-ice accretions (which usually forms between 10 and 20% chord) was largely dependent on its load distribution. The airfoil that was very front-loaded, with large leading-edge suction, had the most severe performance degradation due to this type of ice accretion.

Nomenclature

C_d	=	drag coefficient
$C_{d,\text{clean}}$	=	drag coefficient of clean airfoil
$C_{d,\text{iced}}$	=	drag coefficient of iced airfoil
C_h	=	flap hinge-moment coefficient
C_l	=	lift coefficient
$C_{l,\text{clean}}$	=	lift coefficient of clean airfoil
$C_{l,\text{iced}}$	=	lift coefficient of iced airfoil
$C_{l,\text{max}}$	=	maximum lift coefficient
C_m	=	pitching-moment coefficient
C_p	=	pressure coefficient
$C_{p,\text{min}}$	=	minimum pressure coefficient
c	=	model/airfoil chord length
k	=	protuberance height
M	=	Mach number
Re	=	Reynolds number
r	=	protuberance radius
s	=	model/airfoil coordinate in surface length
t	=	airfoil thickness
x	=	model coordinate in chordwise direction
w	=	protuberance base width
α	=	angle of attack
ΔC_d	=	($C_{d,\text{clean}} - C_{d,\text{iced}}$) at same angle of attack
ΔC_l	=	($C_{l,\text{clean}} - C_{l,\text{iced}}$) at same angle of attack

Introduction

THE critical ice accretion is usually described as the ice formation that causes the maximum degradation in aircraft performance and control. However, accurately determining a critical ice accretion for an aircraft is difficult because the effects of a particular ice accretion on aircraft aerodynamics are dependent on several factors: the ice-accretion geometry, size, and location; the airfoil geometry; aircraft three-dimensional configuration; phase of flight;

and the flight Reynolds and Mach numbers. Determining the relationship between these parameters and their effects on iced-aircraft aerodynamics can lead to an accurate prediction of the critical ice accretion for a particular aircraft, as well as flight conditions to be used in the certification process. Other benefits include incorporating this relationship in the design phase of an airfoil or wing of an aircraft to minimize the sensitivity to icing, as well as improving the accuracy of computational models.

Recent studies at the University of Illinois (Illinois) have attempted to identify the effects of these parameters on iced-aircraft aerodynamics. Lee and Bragg,[1,2] Lee,[3] and Lee and Bragg[4] studied the effects of simulated ridge ice [typically formed in supercooled large droplet (SLD) icing encounters when the ice accretes downstream of the deicing system] on airfoil aerodynamics. The simulated ice shapes were tested on the NACA 23012m (a modified version of NACA 23012), the NLF 0414, and the airfoil sections from a turboprop commuter aircraft currently in service. There were large differences in the iced-airfoil aerodynamics in the four airfoils tested. The most severe performance degradations were observed for the NACA 23012m, with a $C_{l,\text{max}}$ as low as 0.25 for the ice shape with a $k/c = 0.0139$. The effects of the simulated ice shapes were least severe on the NLF 0414, with the lowest $C_{l,\text{max}}$ of 0.68 for the identical ice shape. The effects of ridge ice on the commuter wing and tail airfoils fell in between. The severity of the performance degradation was strongly linked to the location of the ridge ice. Again, the exact nature of the linkage depended greatly on the airfoil geometry. The aerodynamic penalties (in C_l, C_d, C_m, and C_h) were shown to become more severe as the k/c increased from 0.0056 to 0.0139.

Kim and Bragg[5] reported findings on a systematic study of the effect of simulated leading-edge ice-shape geometry on the NLF 0414 airfoil. The ice shapes tested were designed to simulate a single glaze-ice horn with variations in the leading-edge radius, size, and airfoil surface location. The objective of this research was to determine the sensitivity of iced-airfoil aerodynamics to ice-shape geometry. They determined that ice-horn leading-edge radius had only a small effect on airfoil aerodynamics. However, the aerodynamic performance was very sensitive to ice-shape size and location. An almost linear relationship between loss in maximum lift and ice-horn location was found, with the largest loss at the furthest location back on the upper surface. Reynolds number was found to have little effect on the aerodynamic results on the airfoil with simulated ice shapes.

The purpose of the current paper is to provide a summary of the effects of the ice-accretion geometry, size, and location; the airfoil geometry; and the flight Reynolds number on iced-airfoil aerodynamics based on the findings of the recent Illinois

---

*Postdoctoral Research Associate, Department of Aeronautical and Astronautical Engineering, 306 Talbot Lab, 104 South Wright Street. Member AIAA.

†Professor and Head, Department of Aeronautical and Astronautical Engineering, 306 Talbot Lab, 104 South Wright Street. Associate Fellow AIAA.

investigations. When appropriate, the Illinois data will be supplemented by (or compared to) the data that currently exist in the literature to provide a more complete analysis.

Experimental Setup

Two-dimensional airfoil testing was performed in the University of Illinois 3×4 foot Subsonic Wind Tunnel. A detailed description of the experimental methodology is provided in Ref. 3. Four 18-in. chord airfoil models were used: a NACA 23012m model (described in more detail in Ref. 6), an NLF 0414 model, and wing and tail airfoil section models from a commuter aircraft currently in service. The wing airfoil was a modified NACA 63A415, and the tail airfoil was a modified NACA 63A213. A 25% chord simple flap was present on the NACA 23012m and NLF 0414 models (with the hinge located at $x/c = 0.775$). The two commuter models did not have flaps.

The model was attached to a three-component balance that was also used to set the angle of attack. A 0.03-in. gap was present between the model and the floor/ceiling. All of the models had surface pressure taps to measure the pressure distribution. A traverseable wake rake was used to measure the wake pressures, from which the drag was determined.

The lift coefficient C_l and pitching moment coefficient C_m (about the airfoil quarter-chord) measurements were derived from both the force balance and the surface pressure measurements. The integrated surface pressure measurements were used whenever possible because they were generally more accurate due to lower uncertainties (as shown in Table 1). However, because the ice-shape simulations were not instrumented with pressure taps, force balance measurements were used when the ice shapes were tested near the leading edge of the models. Indications of whether the data were obtained from the force balance or the surface pressures will be given later. The drag coefficient C_d measurements were taken with the wake rake. All of the aerodynamic coefficients were corrected for wall effects using the method described by Rae and Pope.[7] Shown in Table 1 are the uncertainty estimates of the aerodynamic coefficients for a typical data point. The case shown is that of the NACA 23012m model with 0.25-in. ridge-ice simulation at $x/c = 0.10$. The model was at $\alpha = 5$ deg with zero flap deflection and $Re = 1.8 \times 10^6$.

The simulated ridge-ice shapes used by Lee and Bragg,[1,2] Lee,[3] and Lee and Bragg[4] were constructed from wooden forward-facing quarter-round shapes of $k/c = 0.0056, 0.0083$, and 0.0139. The $k/c = 0.0139$ shape on the NACA 23012m is shown in Fig. 1. The simulations maintained constant size and shape over the entire span. The boundary layer was tripped at $x/c = 0.02$ on the upper surface and at $x/c = 0.05$ on the lower surface to simulate the residual ice typically found over the airfoil ice protection system.

Table 1 Experimental uncertainties for the NACA 23012m model with 0.25-in. ridge-ice simulation located at $x/c = 0.10$: $\alpha = 5$ deg, $Re = 1.8 \times 10^6$, and $M = 0.18$.

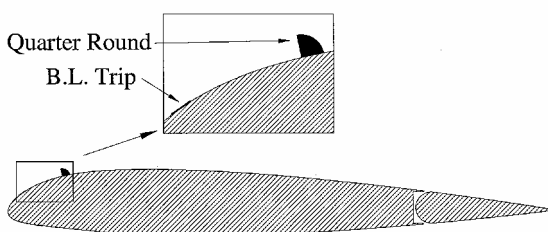| Aerodynamic coefficient	Reference value	Absolute uncertainty	Relative uncertainty, %
C_l pressure	0.282	1.53×10^{-03}	0.54
C_l balance	0.295	1.55×10^{-03}	0.53
C_d wake	0.158	1.47×10^{-03}	0.93
C_m pressure	-0.0787	6.87×10^{-04}	0.87
C_m balance	-0.0791	3.93×10^{-04}	0.50

Fig. 1 NACA 23012m airfoil and spanwise protuberance geometry used by Lee and Bragg.[1]
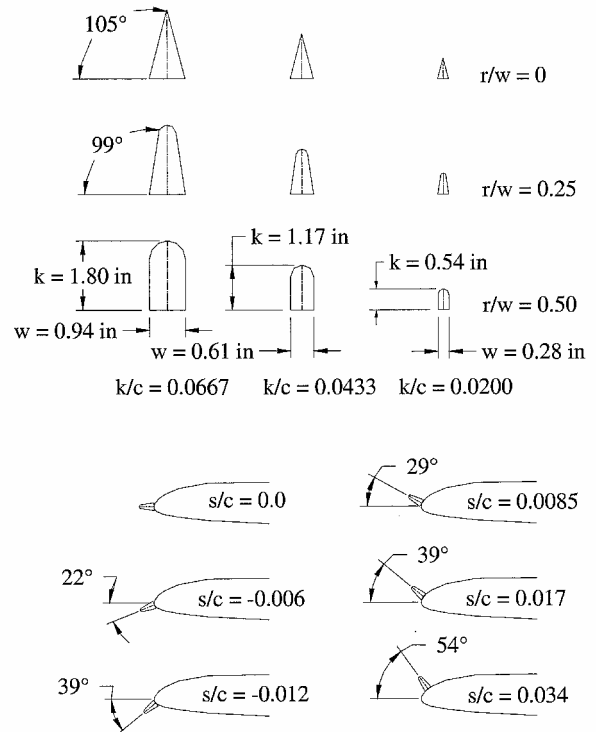

Fig. 2 Simulated glaze-ice shapes and NLF-0414 model used by Kim and Bragg.[5]

A scale drawing of the simulated leading-edge ice shapes and the NLF 0414 model used by Kim and Bragg[5] is shown in Fig. 2. These simulations maintained constant size and shape over the entire span as well. The simulated ice was tested in three heights: $k = 1.2$ ($k/c = 0.0667$), $k = 0.8$ ($k/c = 0.044$), and $k = 0.4$ in. ($k/c = 0.0222$). The simulated ice shapes were tested at six different surface locations between $s/c = 0.012$ on the lower surface and $s/c = 0.034$ on the upper surface (which corresponded to horn angles from -50 to $+60$ deg). The simulated leading-edge glaze-ice geometries were determined from averaging geometry data from a set of actual ice accretions collected from a test at the NASA Glenn Icing Research Tunnel.[8] Leading-edge glaze-ice accretion usually consists of an upper- and a lower-surface horn. However, only the upper-surface ice-accretion geometries were simulated for this research.

Results and Discussion

Brumby[9] provided a generalized summary of the effects of roughness (including icing) on the airfoil maximum lift. This summary showed the relationship between the airfoil maximum lift and the surface disturbance height/location as derived from the existing wind-tunnel data at the time. It showed that increasing the protuberance height and moving it toward the leading edge resulted in increased performance degradation. The relationship was derived primarily form roughness and leading-edge ice simulations. Recent investigations, however, have revealed that this relationship is not valid for large ice accretions.

Effects of Ice-Shape Height

Jacobs[10] reported the effects of various spanwise protuberance heights and locations on the NACA 0012 airfoil. Although these were not tested as ice-shape simulations, the effects on airfoil performance degradation would have been similar to that of ridge ice. The effect of the protuberance height on $C_{l,max}$ exhibited a strong dependence on the ice-shape location, (Fig. 3). When the protuberance was at locations other than the leading edge, the $C_{l,max}$ decreased with increasing protuberance height. When the protuberance was located at the leading edge, the $C_{l,max}$ decreased with increasing k/c until $k/c = 0.005$. When the size of the protuberance was further increased, it had little additional effect on $C_{l,max}$.
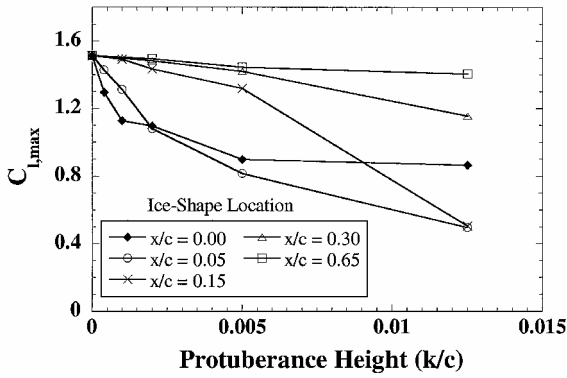
Fig. 3   Variation of maximum lift with spanwise protuberance height on NACA 0012: $Re = 3.1 \times 10^6$ (Ref. 10).
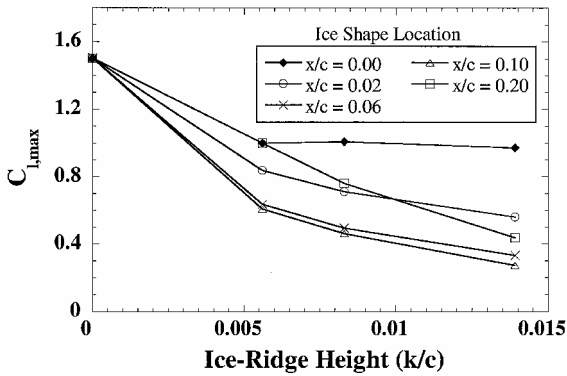

Fig. 4   Variation of maximum lift with simulated ridge-ice height on NACA 23012m: $Re = 1.8 \times 10^6$ (data from pressure measurements).
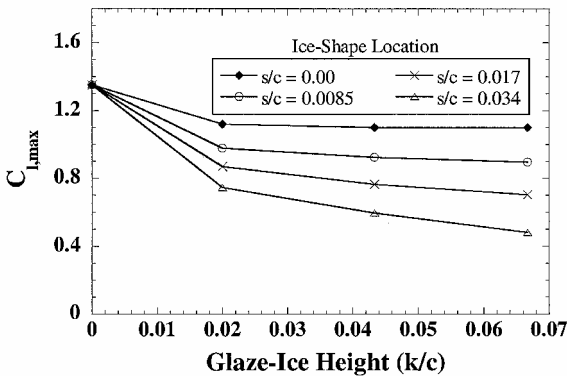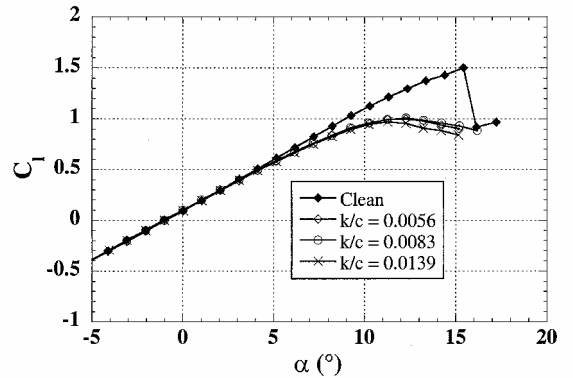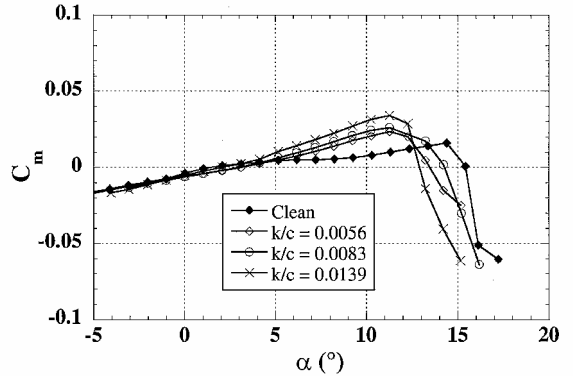

Fig. 5   Variation of maximum lift with simulated glaze-ice height on NLF 0414: $r/w = 0.25$ and $Re = 1.8 \times 10^6$ (data from balance measurements).

a) Lift

b) Pitching moment

Fig. 6   Effect of simulated ridge ice of various heights at the leading-edge location on the NACA 23012m: $Re = 1.8 \times 10^6$ (data from pressure measurements).
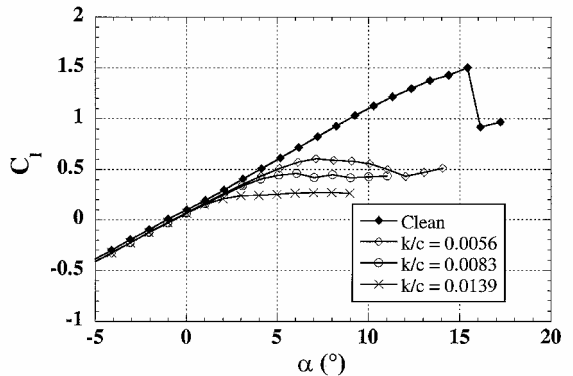

Fig. 7   Effect of simulated ridge ice of various heights at $x/c = 0.10$ location on the NACA 23012m: $Re = 1.8 \times 10^6$ (data from pressure measurements).

Similar behavior was observed on both the simulated ridge ice shapes (Fig. 4) and the leading-edge glaze-ice shapes (Fig. 5) tested at Illinois. Figure 4 shows that when the ridge ice was at and downstream of $x/c = 0.02$, increasing the height resulted in decreased $C_{l,\max}$. When the ridge ice was at the leading edge, increasing the height from $k/c = 0.0056$ to 0.0139 had little effect on $C_{l,\max}$. Figure 5 shows that when the simulated glaze ice was at the leading edge, increasing the height from $k/c = 0.02$–0.067 had almost no effect on $C_{l,\max}$. However, at all other locations, increasing the glaze-ice height resulted in decreased $C_{l,\max}$.

This effect can be examined in more detail through the lift- and pitching-moment plots in Figs. 6a and 6b. Figure 6 shows the effects of simulated ridge ice of various heights (at the leading edge) on lift and pitching moment on the NACA 23012m. Note from Figs. 6 that the height of the simulated shapes made very little difference on the airfoil performance when they were located at the leading edge. The $C_{l,\max}$ varied by less than 10%, even though the height was almost

tripled. The break in the pitching moment (which indicated the onset of stall) for all three heights occurred at 12 deg.

Figure 7 shows the lift data with the simulated ridge ice located at $x/c = 0.10$. The effects of increasing ice-shape height were much more pronounced. The difference in $C_{l,\max}$ between the $k/c = 0.0056$ and 0.0139 shapes was 0.4. Also, increasing the ice-shape height from $k/c = 0.0056$ to 0.0139 decreased the angle at which the break in C_m occurred from 5 to -1 deg.

The height effects were similar for the glaze-horn shapes on the NLF 0414. Figure 8 shows the lift curve with the simulated glaze ice at the leading edge, and Fig. 9 shows the same at $s/c = 0.034$. As shown in Fig. 8, height variations at the leading edge did not cause any appreciable change in $C_{l,\max}$, which remained near 1.1 regardless of height variations ($C_{l,\max} = 1.12$ for $k/c = 0.02$, $C_{l,\max} = 1.09$ for $k/c = 0.0433$, and $C_{l,\max} = 1.10$ for $k/c = 0.0667$). The same was true for α_{stall}, which remained at $\alpha = 9$–10 deg. However, there was a large incremental change in C_m caused by the variation in height,
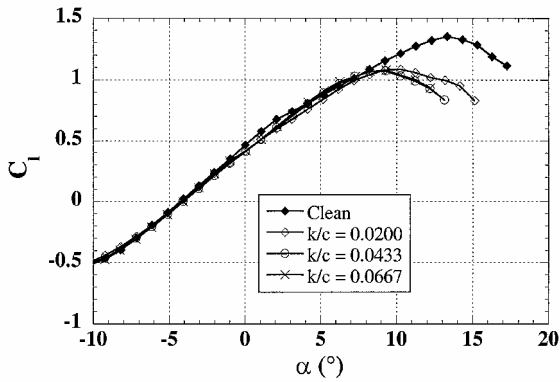
Fig. 8 Glaze-ice simulation height effects on NLF 0414: $s/c = 0.00$, $r/w = 0.25$, and $Re = 1.8 \times 10^6$ (data from balance measurements).
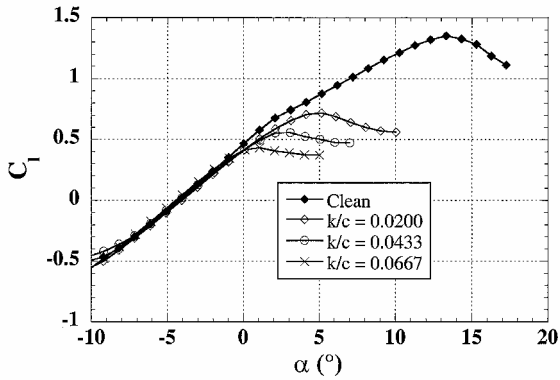

Fig. 9 Glaze-ice simulation height effects on NLF 0414: $s/c = 0.034$, $r/w = 0.25$, and $Re = 1.8 \times 10^6$ (data from balance measurements).

with the pitching moment increasing as the ice height increased for $0 < \alpha < 10$ deg. At $\alpha = 9$ deg, the $k/c = 0.0667$ shape resulted in $C_m = -0.005$; $k/c = 0.0433$ shows $C_m = -0.013$, and $k/c = 0.02$ shows $C_m = -0.031$. This was due to the changes in the flowfield and the effective lengthening of the airfoil chord due to the presence of the ice shape.

At $s/c = 0.034$, the ice-shape height made a significant difference in $C_{l,\max}$ and α_{stall} as shown in Fig. 9. With $k/c = 0.0667$, the $C_{l,\max} = 0.43$ and $\alpha_{\text{stall}} = 1$ deg, which was only about 32% of the clean $C_{l,\max}$ and 12 deg less than the clean α_{stall}. The $k/c = 0.0433$ and 0.02 shapes show $C_{l,\max}$ values of 0.56 and 0.72, respectively, and α_{stall} values of 3 and 5 deg, respectively.

All of the data showed that increasing the ice-shape height generally resulted in more severe performance degradations. The exception to this was when the ice shape was located at the leading edge of the airfoil. After a critical height was reached, further increases in the height did not significantly degrade the performance.

Effects of Ice-Shape Geometry

The glaze horn shapes tested on the NLF 0414 had varying horn radii, as shown in Fig. 2. All of the cases tested had a constant height-to-base ratio of 3.12. For these shapes, the horn radius had very little effect on the iced-airfoil performance. Figure 10 shows the effects of the $k/c = 0.0433$ glaze-ice horn radius on $C_{l,\max}$. It shows that rounding the horn increased $C_{l,\max}$ only slightly. The effects became slightly more pronounced because the ice shape was located further away from the leading edge. When the ice shape was located at the leading edge, the $C_{l,\max}$ remained nearly identical as r/w was increased from 0 to 0.50. The largest increase in $C_{l,\max}$ occurred when the ice shape was located furthest from the leading edge (at $s/c = 0.034$), but this was only a 0.07 increase. The effects of horn leading-edge radius were studied for different ice-shape heights as well and were found to be relatively insensitive to the ice-shape height effects.
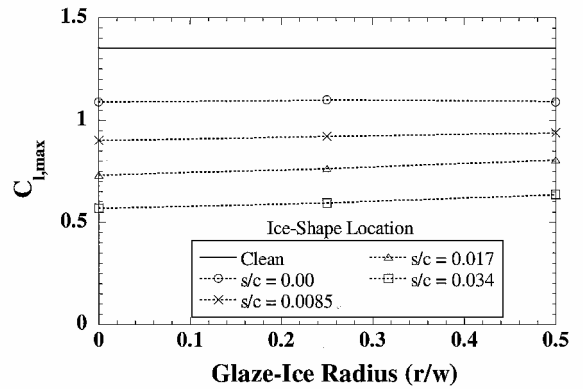

Fig. 10 Glaze-ice simulation horn radius effects on NLF 0414: $k/c = 0.0433$ and $Re = 1.8 \times 10^6$ (data from balance measurements).
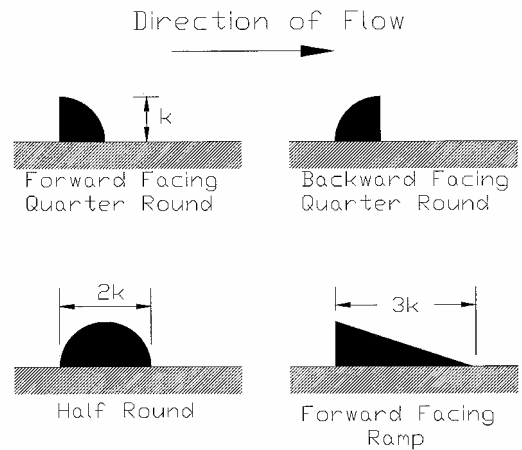

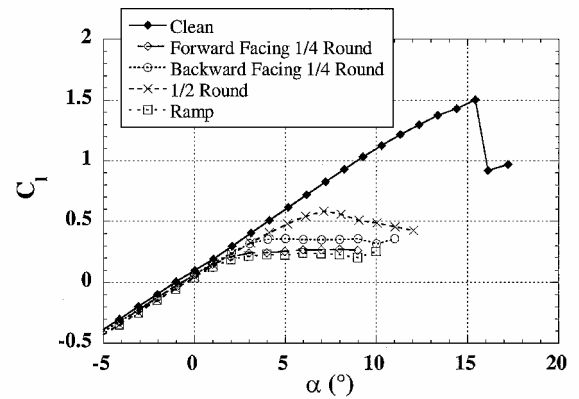**Fig. 11 Ridge-ice simulation geometry tested on NACA 23012m.**

Fig. 12 Effect of simulated ridge-ice geometry on lift (NACA 23012m): $k/c = 0.0139$ simulation height, $Re = 1.8 \times 10^6$ (data from pressure measurements).

Lee and Bragg[1] studied the effects of different types of ridge-ice geometries on the NACA 23012m, as shown in Fig. 11. In addition to the forward-facing quarter-round, the backward-facing quarter-round, half-round, and forward-facing ramp were tested as well. The ramp shape had a base length-to-height ratio of 3.

Figure 12 shows the effect of various ridge-ice geometries (as shown in Fig. 11) on lift. All of the simulations shown in Fig. 11 had $k/c = 0.0139$ and were located at $x/c = 0.10$. Figure 12 shows that varying the ridge-ice geometry did have measurable effects on lift, although they were not usually very large. The forward-facing quarter-round had $C_{l,\max}$ of 0.27, whereas the backward-facing quarter-round has a $C_{l,\max}$ of 0.34. The backward-facing quarter-round had only a slightly less severe effect on lift than the forward-facing quarter-round, even though the side facing the flow

was much more streamlined. The half-round had a significantly higher $C_{l,\max}$ (0.58) than the backward-facing quarter-round, even though they had an identical forward face exposed to the flow. Thus, the geometry of the downstream side can have a significant effect on lift. However, this was the case only when the face exposed to the flow is streamlined (such as with the backward-facing quarter round and the half-round). Figure 12 shows that the forward-facing quarter-round and the ramp shape had nearly identical lift curves, even though they had very different downstream sides. Thus, for the two shapes with very blunt forward faces, the shape of the backward face was not as important (for the shapes tested).

Reynolds Number Effects

When the Reynolds number of a clean airfoil is increased, the $C_{l,\max}$ typically increases as well. This change in $C_{l,\max}$ with Reynolds number can be quite significant on some airfoils. However, on an airfoil with simulated ice, this large effect of Reynolds number has not been observed. Airfoil experiments with surface roughness indicated that once a critical Reynolds number is reached, $C_{l,\max}$ becomes relatively insensitive to further increases in the Reynolds number. This is important because wind-tunnel tests with simulated ice shapes are typically performed at a Reynolds number much lower than that encountered in flight.

Morgan et al.[11] tested frost and ice-shape simulations on a high-lift airfoil in cruise configuration, with the Reynolds numbering varying from 2.8×10^6 to 1.2×10^7. They observed that the maximum lift of the iced airfoil varied by less than 10%, even in this wide range of Reynolds numbers.

Similar results were observed in the Illinois data, although the range of Reynolds numbers tested was much lower. Figure 13 shows the clean and iced-airfoil data for the NLF 0414 at Reynolds numbers of 0.5×10^6, 1.0×10^6, and 1.8×10^6. On the clean airfoil, the $C_{l,\max}$ varied greatly with Reynolds number, even in this limited range. The $C_{l,\max}$ for 0.5×10^6 case was 1.12, whereas $C_{l,\max}$ for the 1.8×10^6 case was 1.35, a difference of 20%.

With the addition of the simulated glaze ice, these Reynolds number effects were greatly reduced. Figure 13 shows the lift curves among the three Reynolds numbers tested were virtually identical. The $C_{l,\max}$ for the $Re = 0.5 \times 10^6$ case was 1.10, for the $Re = 1.0 \times 10^6$ was 1.12, and for the $Re = 1.8 \times 10^6$ case was 1.09 (a maximum difference of 3%). Therefore, $\Delta C_{l,\max}$ between clean and iced configurations may vary with Reynolds number, but the actual $C_{l,\max}$ of the airfoil with the glaze-ice shape remained consistent at least within this Reynolds number range. Similar insensitivity to Reynolds number effects were also observed for drag, pitching moment, and flap-hinge moment.

Figure 14 shows the same trend for the simulated ridge ice on the NACA 23012m. When the Reynolds number was varied from 1.0×10^6 to 1.8×10^6, the change in $C_{l,\max}$ was less than 0.02 for the iced cases, indicating insensitivity to the Reynolds number in this range.

Recent studies by Papadakis et al.[12] and Broeren et al.[13] also showed relative insensitivity of iced-airfoil aerodynamics to
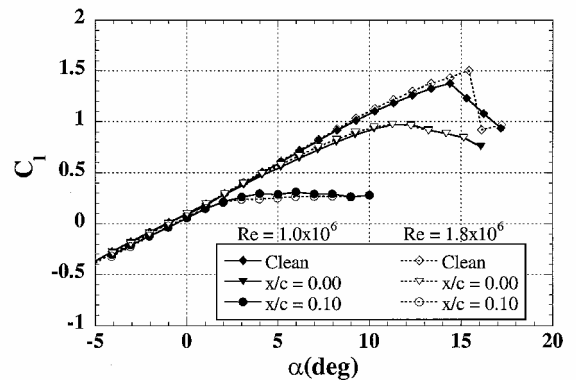
Fig. 14   Reynolds number effect: NACA 23012m, simulated ridge ice, $k/c = 0.0139$ (data from pressure measurements).
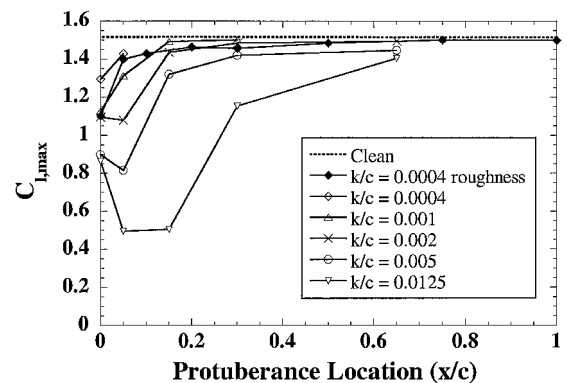
Fig. 15   Effect of protuberance location on maximum lift: NACA 0012; roughness, $Re = 2.88 \times 10^6$ (Gregory[14]); and protuberance $Re = 3.1 \times 10^6$ (Jacobs[10]).

variations in the Reynolds number. Papadakis et al.[12] tested span-wise spoilers to simulate ice accretion on a NACA 0011 model. The results show that as the Reynolds number was increased from 1.36×10^6 to 2.46×10^6, the effect on the lift curve was generally less than 5%. These results were nearly identical to that of the NACA 23012m (Fig. 12). Broeren et al.[13] tested simulated intercycle ice accretions (ice that forms between the deicing boot cycles) on a NACA 23012 airfoil in a pressurized wind tunnel. Both the Reynolds and Mach numbers were controlled in this study. Significant changes in ice-airfoil aerodynamics were not observed as the Reynolds number was varied from 2×10^6 to 1.05×10^7 (at constant Mach number). However, there were slight changes as the Mach number was varied from 0.10 to 0.28 (at constant Reynolds number). This suggested that any slight Reynolds number effect observed in previous studies may have been due to changes in Mach number because this was not held constant.

An implication of the insensitivity of the two-dimensional iced airfoil to the increases in the Reynolds number is that the wind-tunnel data generated at relatively low Reynolds number (less than 2×10^6) can be applied to flight Reynolds number (over 6×10^6) because the results will not vary significantly. Also, this indicates that when the full-size ice shape/airfoil is to be scaled down to be tested using a smaller airfoil at lower Reynolds number, the proper ice-shape scaling is the geometric scaling of k/c.

Effect of Ice-Shape Location

It has previously been assumed that the most critical location (in terms of performance degradation) for the ice accretion was the leading edge of the airfoil.[9] This assumption, however, was largely based on distributed roughness studies that showed that the most severe degradations occurred when the roughness distribution was started at the leading edge of the airfoil.

However, recent Illinois investigations, as well as further analysis of previous experiments, have shown that, for ice accretions, the most critical location is not necessarily the leading edge. Figure 15
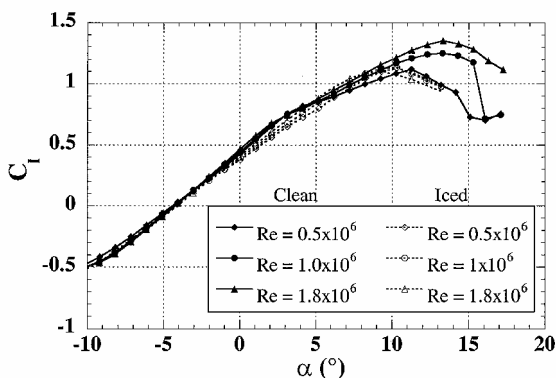
Fig. 13   Reynolds number effects for simulated glaze ice on NLF 0414: $r/w = 0.25$, $s/c = 0.0$, and $k/c = 0.0433$ (data from balance measurements).
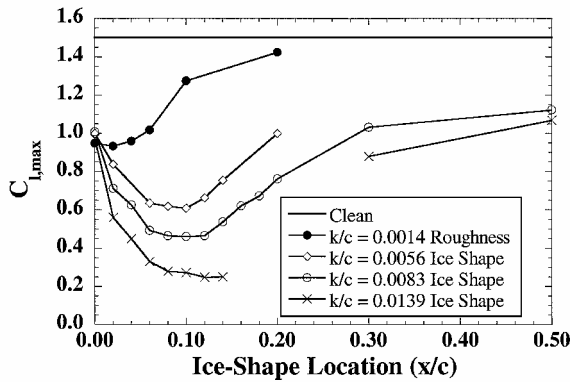
Fig. 16 Summary of maximum lift with simulated ridge ice of various heights: NACA 23012m and $Re = 1.8 \times 10^6$ (data from pressure measurements).

shows the effect of spanwise protuberance location on the maximum lift on the NACA 0012 (as reported by Jacobs[10]). Also plotted in Fig. 15 are the surface roughness results as reported by Gregory and O'Reilly.[14] Figure 15 shows that the most critical protuberance location depends largely on the size. For protuberances of $k/c \le 0.001$ (typical size of roughness), the most critical location was the leading edge. For larger protuberances, the most critical location appears to be between $x/c = 0.05$ and 0.15. Because the tests were only conducted at five chordwise locations, the precise location could not be determined. There also appears to be a trend of the most critical location moving upstream with the decreasing protuberance height. Again, this is not conclusive from Fig. 15 because of the sparseness of the data.

The Illinois tests[1] with simulated ridge ice on the NACA 23012m airfoil yielded similar results. The ice shapes were simulated using a forward-facing quarter-round, as shown in Fig. 1. Figure 16 shows a summary of the $C_{l,max}$ on the NACA 23012m with simulated ridge ice at various chordwise locations. The simulated ice shapes were tested at many more chordwise locations than was done previously to locate the most critical location precisely. Also shown in Fig. 16 is the summary of $C_{l,max}$ with 16-grit roughness ($k/c = 0.0014$). First, note that there are no $C_{l,max}$ results shown between $x/c = 0.14$ and 0.30 for the $k/c = 0.0139$ ice shape. This was because a distinct $C_{l,max}$ in the traditional sense was not observed at these locations for this ice shape. Instead, there was simply an inflection in the lift curve when the flow downstream of the ice shape had become fully separated. However, the flow ahead of the ice shape was still fully attached, increasing lift with increasing angles of attack (although at a much reduced rate).

On the NACA 23012m, the most critical location for the ice shape was not at the leading edge, but at $x/c = 0.14$ (for $k/c = 0.0139$), $x/c = 0.12$ (for $k/c = 0.0083$), and $x/c = 0.10$ (for $k/c = 0.0056$). When the ridge ice was located upstream of this location, the separation bubble that formed downstream of the ice shape was not very large. (It is important to distinguish this bubble from the classic laminar separation bubble that forms on airfoils at low Reynolds numbers. Structurally, it is more similar to a recirculation region downstream of a backward-facing step.) This was because the ice shape was located in a favorable pressure gradient, ahead of the pressure recovery. When the ridge ice was located downstream of this location, a significant amount of lift was still generated from the attached region upstream of the ice shape. When the ridge ice was located in the critical location of $x/c = 0.10$–0.14, the separation bubble that formed downstream of the ice shape eliminated the large leading-edge suction peak of the clean model, from which most of the lift on the NACA 23012m was generated. This is explained in greater detail by Lee and Bragg.[1]

Figure 16 shows that the most critical location moves upstream with decreasing ice-shape height, but that the shift was not large over this size range. For the distributed roughness (with $k/c = 0.0014$), the most critical location was at $x/c = 0.02$, much closer to the leading edge. This was because the distributed roughness had an

effect that was quite different than that of the ridge ice. The ridge ice induced early stall through the formation of a separation bubble that grew rapidly with increasing angle of attack. The roughness, however, extracted momentum from the boundary layer, resulting in early transition and separation. Because of this, the largest loss in momentum occurred when the roughness was located near the leading edge (which coincided with the lowest $C_{l,max}$).

Bowden[15] speculated that the most critical ice-accretion location, in terms of drag increase, was the location of the maximum local air velocity (or $C_{p,min}$) of the clean airfoil. Lee and Bragg[1] speculated that the ice accretion would extract the greatest amount of boundary-layer momentum at this location. Similarly, they also thought that the most critical ice-accretion location, in terms of lift and pitching moment, was closely related to the location of $C_{p,min}$ and the maximum adverse pressure gradient downstream of $C_{p,min}$. The large performance degradations due to ice accretion are primarily due to the large separation bubble that forms downstream of the ice. It was believed that the largest separation bubbles would form when the ice accretion was located near the location of $C_{p,min}$, placing the separation bubble in the region of maximum adverse pressure gradient.

A new analysis of Jacobs's data[10] and the Illinois results of Lee and Bragg[1] showed that, for NACA 0012 and NACA 23012m airfoils, the critical ice-accretion location was often related to the location of $C_{p,min}$ and the maximum adverse pressure gradient.

Figure 17 shows the ΔC_l (lift loss due to the $k/c = 0.0014$ roughness and $k/c = 0.0139$ ridge ice when compared to the clean airfoil at the same angle of attack) on the NACA 23012m. Each curve represents a fixed angle of attack, and the spanwise protuberance location is depicted on the x axis. Also shown in Fig. 17 by the solid arrows are the locations of maximum local air velocity (or $C_{p,min}$) of the clean airfoil for each angle of attack. The open arrows are the location of the maximum adverse pressure gradient (also of the clean airfoil). The most critical location of the roughness varied between $x/c = 0.02$ for $\alpha = 3$ deg to $x/c = 0.06$ for $\alpha = 8$ deg. For the ridge ice, the most critical location was between $x/c = 0.10$ and 0.12 and did not vary significantly with angle of attack. For the roughness, the most critical location appeared to be slightly downstream of the location of the maximum local air velocity. For the ridge ice, the most critical location was situated between the locations of the maximum local air velocity and the maximum adverse pressure gradient. Thus, it did appear that the most critical simulated ice-shape location was related to these flow features.

Figure 18 shows the drag increase due to roughness ($k/c = 0.0014$) and spanwise ridge-ice simulation ($k/c = 0.0139$) on the NACA 23012m. It shows that the most critical location moved upstream with increasing angles of attack and closely coincided with the location of the maximum local air velocity. This appeared to validate the observation reported by Bowden.[15]

The results from the NACA 0011 and NACA 23012m showed that, for these two airfoils, the ridge-ice location that resulted in the most severe performance degradation was related to the location of
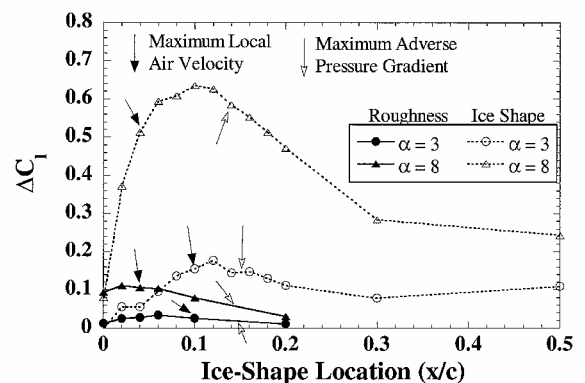

Fig. 17 Lift loss due to surface roughness ($k/c = 0.0014$) and simulated ridge ice ($k/c = 0.0139$): NACA 23012m and $Re = 1.8 \times 10^6$ (data from pressure measurements).
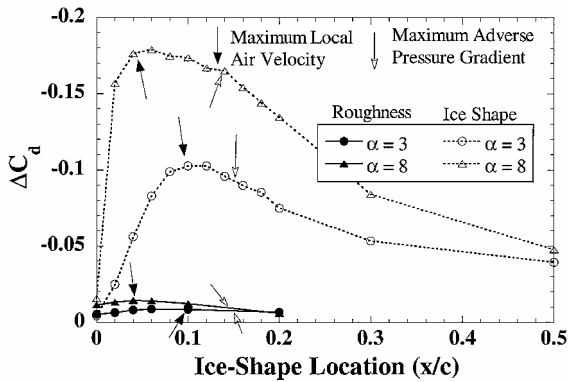
Fig. 18   Drag increase due to surface roughness ($k/c = 0.0014$) and simulated ridge ice ($k/c = 0.0139$): NACA 23012m and $Re = 1.8 \times 10^6$.
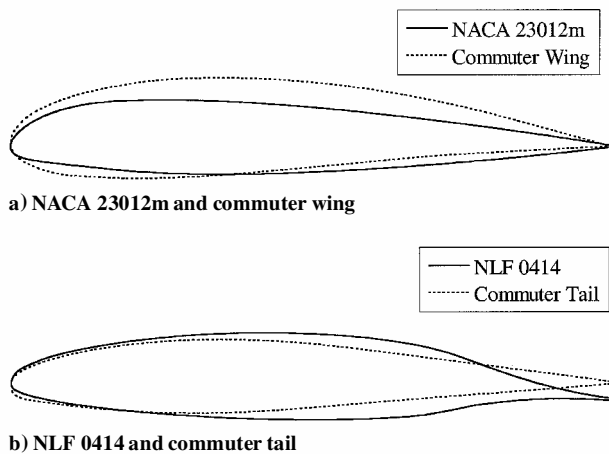

a) NACA 23012m and commuter wing

b) NLF 0414 and commuter tail

Fig. 19   Geometry comparison of four airfoils tested at Illinois.

a) NACA 23012m ($\alpha = 4.12$ deg) and commuter wing ($\alpha = 1.02$ deg)

b) NLF 0414 ($\alpha = 0.02$ deg) and commuter tail ($\alpha = 3.07$ deg)

Fig. 20   Clean-model surface pressure comparison, $C_l = 0.5$.

the maximum local air velocity and the maximum adverse pressure gradient of the clean airfoil. In fact, the most critical location in terms of drag coincided very well with the location of the maximum local air velocity. However, tests with other airfoils showed that this relationship did not exist for other types of airfoils.

Effect of Airfoil Geometry

In the preceding section, it was shown that the aerodynamic effects of protuberance on the NACA 0012 and the NACA 23012m were very similar. This is not surprising, because although NACA 23012m is cambered and NACA 0012 is not, they have identical thickness distributions.[16] It was shown by Lee and Bragg[4] that the effects of simulated ice can depend greatly on airfoil geometry. Those results are reviewed and explained in this section.

Identical ridge-ice geometry (the forward-facing quarter-round) was tested on four airfoils: NACA 23012m, NLF 0414, and wing and tail airfoil sections from a commuter-class aircraft currently in service. The geometries of these airfoils are shown in Fig. 19. The commuter wing was the thickest airfoil tested ($t/c = 0.16$). The commuter tail was the thinnest airfoil ($t/c = 0.11$). The commuter wing and NLF 0414 were highly cambered, whereas the NACA 23012m and the commuter tail were only moderately cambered.

The different aerodynamic characteristics are very apparent in the measured clean-model surface pressure distribution of Fig. 20. In Fig. 20, the surface pressures are compared at nearly identical lift coefficients of 0.5. Because of varying degree of camber, each airfoil was at a different angle of attack. On the NLF 0414 and NACA 23012m, there was a pressure discontinuity near $x/c = 0.76$ due to the flap gap on the models. This was not present on the commuter wing and tail sections because these models were not flapped.

The NACA 23012m has a very large suction peak (with $C_{p,\min} = -1.4$) centered near $x/c = 0.08$. There was a severe pressure recovery (with very adverse pressure gradient) from $x/c = 0.08$–0.22.
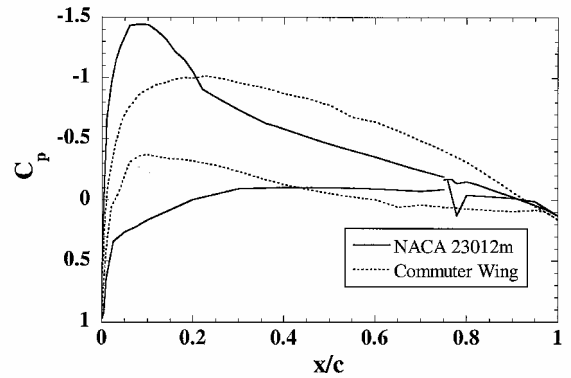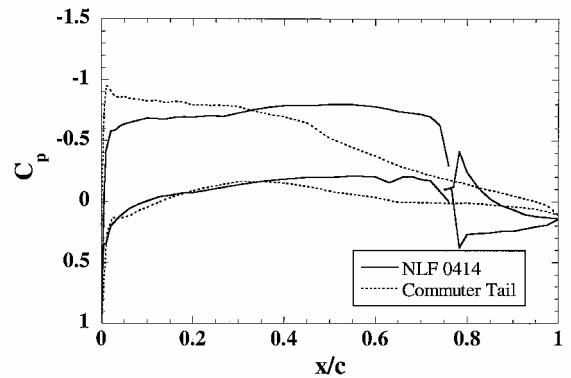
The pressure recovery became more gradual downstream of this location and extended to the trailing edge.

The commuter wing airfoil had a pressure distribution that was quite different. A large suction peak was not present on this airfoil at this angle of attack, with a $C_{p,\min}$ value of -0.93 located at $x/c = 0.23$. Because a large suction peak was not present, the pressure recovery was very gradual, with a nearly constant pressure gradient extending from $x/c = 0.25$ to 0.80. The pressure gradient became more adverse between $x/c = 0.80$ and the trailing edge.

The NLF 0414 had a nearly constant C_p between $x/c = 0.04$ and 0.72. The pressure recovery did not start until $x/c = 0.72$. Because of the short recovery region, the adverse pressure gradient in this region was the most severe of the four airfoils tested.

The commuter tail airfoil was similar to the NLF 0414 in that the C_p was relatively constant (with a slight adverse gradient) between $x/c = 0.03$ and 0.45, with most of the recovery occurring between $x/c = 0.45$ and the trailing edge. Because the pressure recovery region on the commuter tail was larger than on the NLF 0414, the adverse pressure gradient was not as severe.

Figure 21 shows a summary of $C_{l,\max}$ as a function of the ridge-ice location for the four airfoils tested. The airfoil models were tested with ice shapes located as far downstream as midchord. However, only the data points for which a clear $C_{l,\max}$ existed are shown. As stated earlier, on the NACA 23012m, a $C_{l,\max}$ in the traditional sense was not observed when the ridge ice was located between $x/c = 0.14$ and 0.30. Figure 21 shows that, generally, moving the ridge ice downstream resulted in larger degradations of maximum lift (the exception being the NACA 23012m). For all four airfoil models, the highest $C_{l,\max}$ was observed when the ridge ice was located at the leading edge. The NACA 23012m was most sensitive to the ridge-ice location in the first 15% chord. This was followed by the commuter wing, the commuter tail, and the NLF 0414. There was little variation in $C_{l,\max}$ when the ridge-ice location was varied between $x/c = 0.02$ and 0.20 on the NLF 0414 and the commuter tail. However, on the NACA 23012m and the commuter wing, moving the ridge ice from $x/c = 0.02$ to 0.20 caused significant reductions in the maximum lift.
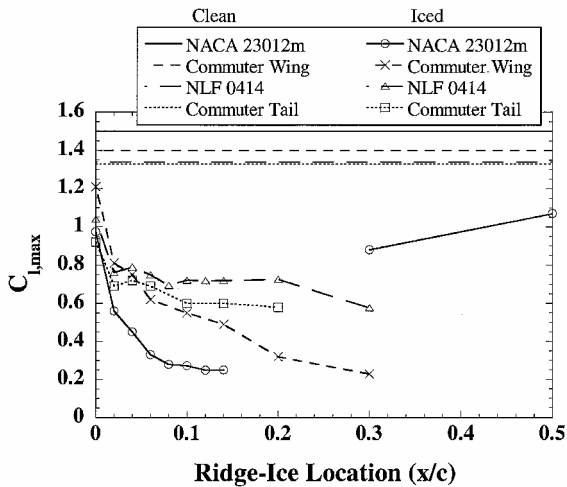
Fig. 21 Effect of ridge-ice location on maximum lift: $k/c = 0.0139$ and $Re = 1.8 \times 10^6$ (data from pressure measurements).

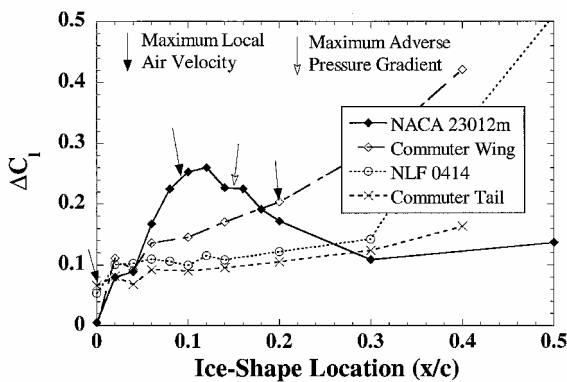**Fig. 22 Effect of ridge-ice location on lift loss; $Re = 1.8 \times 10^6$ and $C_{l,\text{clean}} \cong 0.5$: NACA 23102 $\alpha = 4$, commuter wing $\alpha = 1$, NLF 0414 $\alpha = 0$, and commuter tail $\alpha = 3$ deg (data from pressure measurements).**
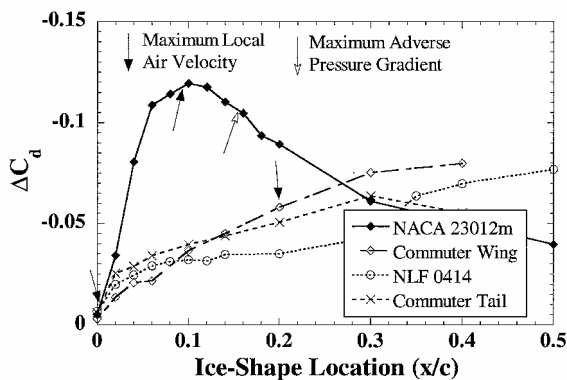

Fig. 23 Effect of ridge-ice location on drag increase; $Re = 1.8 \times 10^6$ and $C_{l,\text{clean}} \cong 0.5$: NACA 23102 $\alpha = 4$, commuter wing $\alpha = 1$, NLF 0414 $\alpha = 0$, and commuter tail $\alpha = 3$ deg.

Figures 22 and 23 show the effect of the ridge-ice location on the change in the integrated coefficients from the clean model values. Figure 22 shows ΔC_l ($C_{l,\text{clean}} - C_{l,\text{iced}}$), or the lift loss compared to the clean airfoil, due to the simulated ridge ice. Each curve represents a fixed angle of attack, and the simulated ice-shape location is depicted on the x axis. The angle of attack shown for the four airfoils corresponded to that of the clean airfoil at a nominal C_l value of 0.50 to provide a fair comparison. Shown in Fig. 22 by the solid arrows are the locations of maximum local air velocity, or $C_{p,\text{min}}$ (of the clean airfoil), for each angle of attack. The open arrows are the location of the maximum adverse pressure gradient (also of the clean airfoil). On the NACA 23012m, the largest lift loss occurred when

the ice shape was located at $x/c = 0.12$ and was located between the maximum local air velocity and the maximum adverse pressure gradient. The $x/c = 0.12$ ice-ridge location was near the same x/c location that produced the lowest $C_{l,\text{max}}$, as shown in Fig. 21.

On the commuter wing, the maximum local air velocity was located at $x/c = 0.20$. The maximum adverse pressure gradient was located at $x/c = 0.90$ and is not shown in Fig. 22. Moving the ridge ice downstream increased the loss in lift. This trend continued as far off ($x/c = 0.50$) as the simulated ridge ice was tested.

On the NLF 0414, the maximum local air velocity was located at $x/c = 0.55$, and the maximum adverse pressure gradient was located at $x/c = 0.75$. Neither of these locations is shown in Fig. 22. When the ridge ice was located between $x/c = 0.02$ and 0.30, there was little change in ΔC_l with ridge-ice location. When the ridge ice was located at $x/c = 0.02$, ΔC_l was 0.10, and when the ridge ice was located at $x/c = 0.30$, ΔC_l was 0.14, an increase of 40%. In the same x/c range, ΔC_l increased by 260% on the commuter wing airfoil. When the ridge ice was located downstream of $x/c = 0.30$ on, there was a much larger increase in lift loss as the ridge ice was moved downstream.

On the commuter tail airfoil, the maximum local air velocity was located very near the leading edge at $x/c = 0.01$. The maximum adverse pressure gradient was located at $x/c = 0.50$. As the ridge-ice location was varied from the leading edge to $x/c = 0.40$, there was a gradual increase in ΔC_l, with values very similar to that of the NLF 0414. Unlike on the NLF 0414, there was not a sudden increase in ΔC_l downstream of $x/c = 0.30$.

Figure 23 shows the change in drag ΔC_d ($C_{d,\text{clean}} - C_{d,\text{iced}}$) compared to the clean airfoil due to the 0.25-in. ridge-ice simulation. Again, solid arrows show the location of the maximum local air velocity and the open arrows show the location of the maximum adverse pressure gradient. On the NACA 23012m, there was a large increase in the magnitude of ΔC_d as the ridge-ice location was moved downstream from the leading edge. The peak value in drag rise occurred when the ridge was located at $x/c = 0.10$, which coincided with the location of the maximum local air velocity. As the ridge ice was moved downstream of this location, the magnitude of ΔC_d decreased.

On the commuter wing, the magnitude of ΔC_d increased as the ridge ice was moved downstream, in manner similar to that observed for lift (Fig. 22). On the NLF 0414, as the ridge ice was moved downstream from $x/c = 0.02$ to 0.30, there was a gradual increase in the magnitude of ΔC_d (approximately one-third of the rate observed on the commuter wing). As with lift, there was a sudden increase in the magnitude of ΔC_d at $x/c = 0.30$. The commuter tail exhibited similar characteristics, except that there was a decrease in the magnitude of ΔC_d when the ridge ice was moved downstream of $x/c = 0.30$.

The results of Figs. 22 and 23 showed that, except for drag on the NACA 23012m, the critical ridge-ice location where the maximum changes in C_l and C_d occurred were not precisely related to the location of the maximum local air velocity and the maximum adverse pressure gradient of the clean airfoil. The ridge-ice location where the maximum changes in lift and drag occurred appeared to be only loosely related to where the maximum adverse pressure gradient was located.

The differences in the sensitivity of the airfoils to the ridge-ice location was attributed to the differences in the clean-model pressure distributions (Fig. 20). Generally, the severity of the effect of ridge ice is directly related to the length of the separation bubble that forms downstream of the ice shape. This, in turn, is determined primarily by the severity of the adverse pressure gradient downstream of the ice shape, over which the bubble is forced to reattach. A more severe adverse gradient typically results in a longer separation bubble. The effect of ridge ice on surface pressure distribution is shown in Fig. 24. All of the clean models are at $C_l = 0.5$, which explains the various angles of attack. Before the iced-airfoil pressure distribution is discussed, it is important to understand the basic features. Figure 24b shows the pressure distribution on the commuter wing airfoil with the ridge ice at $x/c = 0.10$. On the upper surface, the C_p decreased as the flow initially accelerated from the leading
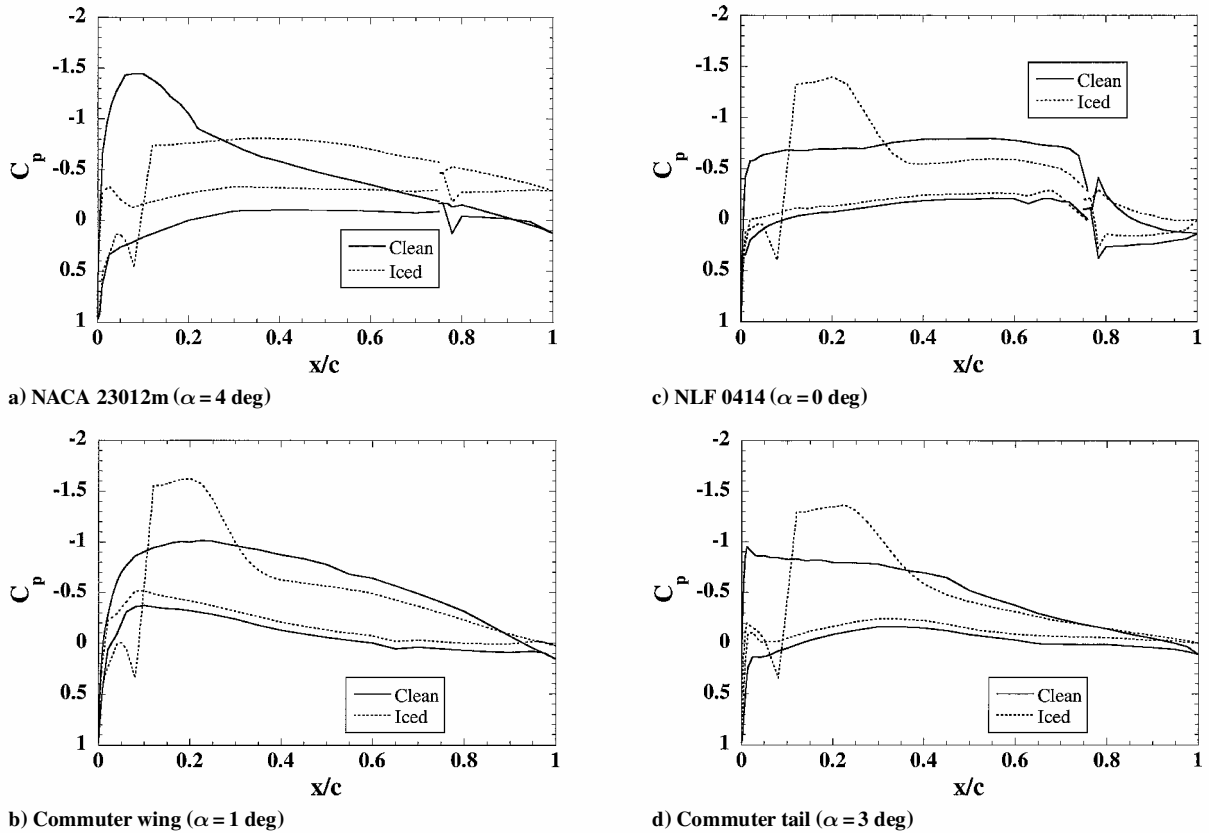
a) NACA 23012m (α = 4 deg)

b) Commuter wing (α = 1 deg)

c) NLF 0414 (α = 0 deg)

d) Commuter tail (α = 3 deg)

Fig. 24   Effect of ridge ice on surface pressure distribution; ridge ice at x/c = 0.10, Re = 1.8 × 10^6, clean model C_l = 0.5.

edge to $x/c = 0.06$, where it started to decelerate as it encountered an adverse pressure gradient due to the ridge ice. The flow then accelerated again over the ridge ice and separated, resulting in a region of relatively constant C_p between $x/c = 0.10$ and 0.22. The C_p then increased as the reattachment process began. The reattachment occurred where the iced C_p value approached the clean value and started to take on a similar form, at $x/c = 0.35$. A more complete description of the iced-airfoil pressure distribution can be found in Ref. 1.

Figure 24a shows why the NACA 23012m was the most sensitive airfoil when the ridge ice was located in the first 20% chord. Because the NACA 23012m had a large suction peak near the leading edge, it also had a very severe pressure recovery region that extended from $x/c = 0.10$ to 0.20. If an ice shape was located upstream of $x/c = 0.20$, the resulting separation bubble would be located in this region of very adverse pressure gradient. The bubble cannot easily reattach in this region, resulting in a long bubble. This is shown on Fig. 24a, where the ridge ice was located at $x/c = 0.10$. The pressure distribution on the upper surface of the iced airfoil did not approach the clean case after the initial separation over the ice shape. This indicated that the bubble failed to reattach on the airfoil (which was confirmed by flow visualization).

The adverse gradient on the commuter wing was not as severe as that on the NACA 23012m. Thus, the separation bubble that formed downstream of the ice shapes was not as large, resulting in less lift degradation. (Note that lift was actually increased in the region of the bubble when compared to the clean case. However, before and aft of the bubble, the lift was decreased due to the global effect of the bubble on the airfoil flowfield and circulation. The loss in airfoil lift increased with the size of the bubble.) This is shown in Fig. 24b. The bubble appeared to have reattached at $x/c = 0.35$.

The separation bubble or recirculation region aft of the ice shape forms due to a large, local adverse pressure gradient imposed on the boundary layer over the ice shape. The separated shear layer thus recovers this local pressure rise, but over a larger distance. In addition, the bubble resides in a global flowfield imposed by the overall airfoil flow that may impose an additional pressure gradient, favorable

or unfavorable, on the bubble shear layer. Thus, the local ice-shape flowfield and the global, clean-airfoil flowfield in a sense interact to produce the final iced-airfoil pressure distribution and integrated forces and moments. The pressure distribution on the NLF 0414 is shown on Fig. 24c and demonstrates the influence of the global or clean-airfoil flowfield on the bubble size and iced-airfoil pressure distribution. On the clean model, the adverse gradient (where the recovery took place) on the NLF 0414 did not begin until $x/c = 0.74$. Ahead of the recovery region, the pressure gradient was nearly zero. Because of this, the lift was relatively insensitive to the ice-shape location because the bubble was not required to recover additional pressure by the imposed clean airfoil flowfield. It was not until the ridge ice was located at $x/c = 0.30$ that the bubble encountered the adverse gradient and that the maximum lift started to experience an additional penalty. When the ridge ice was located at $x/c = 0.10$, the bubble reattached at $x/c = 0.35$.

The commuter tail airfoil was similar to the NLF 0414 in that there was a region of nearly constant surface pressure extending from the leading edge, as shown on Fig. 24d. However, this extended to only $x/c = 0.45$. Most of the pressure recovery occurred downstream of $x/c = 0.45$, where there was a more severe adverse gradient. When the ridge ice was located at $x/c = 0.10$, the bubble reattached at $x/c = 0.40$. Figure 24 shows that the commuter tail was slightly more sensitive to the ridge location than the NLF 0414 because of the slight adverse pressure gradient present between $x/c = 0.03$ and 0.45. However, it was less sensitive than either the NACA 23012m or commuter wing airfoil due to the region of nearly constant pressure.

The results shown indicated that, generally, the more front loaded the airfoil was (with large leading-edge suction peak), the more sensitive it was to SLD-type ridge-ice accretion. Of the four airfoils tested, the NACA 23012m was the most front loaded, with the largest suction peak. It had the largest performance degradation due to ridge-ice accretion, especially in the 10–20% chord range where it is likely to occur. The NLF 0414, which was the most aft loaded of the airfoils tested, was the most insensitive to SLD ridge-ice accretion. The two commuter airfoils fall in between the

NACA 23012m and NLF 0414 in terms of their front loadedness. The performance degradations on the commuter airfoils, thus, fall in between the NACA 23012m and NLF 0414.

Summary

This paper provided a review of findings from recent Illinois investigations on the effects of icing on airfoil aerodynamics. More specifically, the effects due to the following parameters were reviewed: the ice-accretion geometry, size, and location; the airfoil geometry; and the Reynolds number. The review was also supplemented with data that currently exist in the literature to provide a more complete analysis. The following conclusions can be drawn from this research:

1) Increasing the ice-shape height generally resulted in more severe performance degradation. The exception was when the ice shape was located at the leading edge of the airfoil. After a critical height was reached, further increases in the height did not significantly degrade performance.

2) Varying the glaze-ice horn leading-edge radius did not have a large effect on airfoil performance. The effects were most pronounced for positions furthest away from the leading edge of the airfoil and did not depend on the ice-shape height.

3) The variations in the geometry of the simulated ridge ice had some effect on airfoil aerodynamics, with (of the shapes tested) the half-round shape having a significantly higher $C_{l,\max}$.

4) Iced-airfoil aerodynamics were relatively insensitive to Reynolds number variations.

5) Large differences in iced-airfoil aerodynamics were observed between different airfoil geometries. The findings showed that an airfoil's sensitivity to SLD ridge-ice accretion (which usually forms between 10–20% chord) was largely dependent on its load distribution. The airfoil that was very front loaded, with large leading-edge suction, had the most severe performance degradation due to SLD-type ice accretion. In contrast, the most aft loaded airfoil, with favorable, or zero, pressure gradient near the leading edge was the least sensitive to SLD-type ice accretion.

References

[1]Lee, S., and Bragg, M. B., "Experimental Investigation of Simulated Large-Droplet Ice Shapes on Airfoil Aerodynamics," *Journal of Aircraft*, Vol. 36, No. 5, 1999, pp. 844–850

[2]Lee, S., and Bragg, M. B., "Effects of Simulated Spanwise-Ice Shapes on Airfoils: Experimental Investigation," AIAA Paper 99-0092, Jan. 1999.

[3]Lee, S., "Effects of Supercooled Large Droplet Icing on Airfoil Aerodynamics," Ph.D. Dissertation, Dept. of Aeronautical and Astronautical Engineering, Univ. of Illinois at Urbana–Champaign, Urbana, IL, May 2001.

[4]Lee, S., and Bragg, M. B., "The Effect of Ridge–Ice Location and the Role of Airfoil Geometry," AIAA Paper 2001-2481, June 2001.

[5]Kim, H. S., and Bragg, M. B., "Effects of Leading-Edge Ice Accretion Geometry on Airfoil Performance," AIAA Paper 99-3150, June–July 1999.

[6]Lee, S., Dunn, T., Gurbacki, H. M., Bragg, M. B., and Loth, E., "An Experimental and Computational Investigation of Spanwise-Step-Ice Shapes on Airfoil Aerodynamics," AIAA Paper 98-0490, Jan. 1998.

[7]Rae, W. H., and Pope, A., *Low-Speed Wind Tunnel Testing*, Wiley, New York, 1984, pp. 344–362.

[8]Shin, J., and Bond, T. H., "Repeatability of Ice Shapes in the NASA Lewis Icing Research Tunnel," *Journal of Aircraft*, Vol. 31, No. 5, 1994, pp. 1057–1063.

[9]Brumby, R. E., "The Effect of Wing Contamination on Essential Flight Characteristics," *SAE Aircraft Ground De-Icing Conference*, Douglas Paper 8127, Denver, Sept. 1988.

[10]Jacobs, E. N., "Airfoil Section Characteristics as Affected by Protuberances, NACA Rept. 446, 1932.

[11]Morgan, H. L., Ferris, J. C., and McGhee, R. J., "A Study of High-Lift Airfoils at High Reynolds Number in the Langley Low-Turbulence Pressure Tunnel," NASA TM-89125, July 1987.

[12]Papadakis, M., Alansatan, S., and Seltman, M., "Experimental Study of Simulated Ice Shapes on a NACA 0011 Airfoil," AIAA Paper 99-0096, Jan. 1999.

[13]Broeren, A. P., Addy, H. E., and Bragg, M. B., "Effect of Intercycle Ice Accretions on Airfoil Performance," AIAA Paper 2002-0240, Jan. 2002.

[14]Gregory, N., and O'Reilly, C. L., "Low-Speed Aerodynamic Characteristics of NACA 0012 Aerofoil Section, Including the Effects of Upper-Surface Roughness Simulating Hoar Frost," Aeronautical Research Council, ARC R&M 3726, Jan. 1970.

[15]Bowden, D. T., "Effect of Pneumatic De-Icers and Ice Formations on Aerodynamic Character of an Airfoil," NACA TN 3564, Feb. 1956.

[16]Abbott, I. H., and von Doenhoff, A. E., *Theory of Wing Sections*, Dover, New York, 1959, pp. 113–116.